Journal of Alloys and Compounds 512 (2012) 85–93

Contents lists available at SciVerse ScienceDirect

Journal of Alloys and Compounds

journal homepage: www.elsevier.com/locate/jallcom

Microstructural characterization and amorphous phase formation in $Co_{40}Fe_{22}Ta_8B_{30}$ powders produced by mechanical alloying

Amir Hossein Taghvaei[a,*], Mihai Stoica[b], Gavin Vaughan[c], Mohammad Ghaffari[d], Saeed Maleksaeedi[e], Kamal Janghorban[a]

[a] Department of Materials Science and Engineering, School of Engineering, Shiraz University, Shiraz, Iran
[b] IFW Dresden, Institute for Complex Materials, Helmholtzstr. 20, D-01069 Dresden, Germany
[c] ESRF, F-38042 Grenoble, France
[d] School of Electrical & Electronic Engineering, Nanyang Technological University, Nanyang Avenue, Singapore 639798, Singapore
[e] Singapore Institute of Manufacturing Technology, 71 Nanyang Drive, Singapore 638075, Singapore

ARTICLE INFO

Article history:
Received 26 July 2011
Received in revised form 6 September 2011
Accepted 8 September 2011
Available online 16 September 2011

Keywords:
Mechanical alloying
X-ray diffraction
Amorphization

ABSTRACT

In this work, microstructural evolution and amorphous phase formation in $Co_{40}Fe_{22}Ta_8B_{30}$ alloy produced by mechanical alloying (MA) of the elemental powder mixture under argon gas atmosphere was investigated. Milling time had a profound effect on the phase transformation, microstructure, morphological evolution and thermal behavior of the powders. These effects were studied by the X-ray powder diffraction (XRD) in reflection mode using Cu Kα and in transmission configuration using synchrotron radiation, transmission electron microscopy (TEM), scanning electron microscopy (SEM) and differential scanning calorimetry (DSC). The results showed that at the early stage of the milling, microstructure consisted of nanocrystalline bcc-(Fe, Co) phases and unreacted tantalum.

Further milling, produced an amorphous phase, which became a dominant phase with a fraction of 96 wt% after 200 h milling. The DSC profile of 200 h milled powders demonstrated a huge and broad exothermic hump due to the structural relaxation, followed by a single exothermic peak, indicating the crystallization of the amorphous phase. Further XRD studies in transmission mode by synchrotron radiation revealed that the crystalline products were $(Co, Fe)_{20.82}Ta_{2.18}B_6$, $(Co, Fe)_{21}Ta_2B_6$, and $(Co, Fe)_3B_2$. The amorphization mechanisms were discussed in terms of severe grain refinement, atomic size effect, the concept of local topological instability and the heat of mixing of the reactants.

1. Introduction

In the recent years, amorphous alloys have become increasingly attractive due to their potential applications and variety of unique properties like mechanical, corrosion and magnetic behavior. Their excellent properties are attributed to the absence of the atomic long range order and crystalline defects like dislocations and grain boundaries [1–5].

Amorphous alloys can be produced by several methods, such as rapid solidification, severe plastic deformation and solid state processing [2–5]. The size or thickness of the rapidly quenched ordinary amorphous alloy is usually limited to a few microns in the shape of ribbon or sheets [6]. During the preparation of these alloys, a high cooling rates (10^6 K/s) are required to avoid crystallization [6]. In order to enhance the glass forming ability and increase the dimensions, multicomponent bulk metallic glasses have been developed. These alloys have low critical cooling rates (10^3 K/s), under which fully amorphous products with the thickness of 70 mm have been produced [7].

Mechanical alloying (MA) is an alternative process to produce amorphous alloys from the elemental powders. It has been found that MA has some advantages in comparison with the conventional casting or rapid solidification methods. The mechanically alloyed amorphous powders could easily be consolidated in the supercooled liquid region into high density bulk amorphous samples with arbitrary shapes and dimensions without any finishing process like machining [8]. Besides, MA is versatile enough to allow amorphization in the compositional ranges wider than those corresponding to the rapid solidification which are close to the eutectic composition [5,8]. On the other hand, the most important disadvantage of the MA process is the introduction of contamination and milling debris into the powders from balls or milling medium, which can affect the thermal stability and some physical properties of amorphous powder. Formation of amorphous phases by MA depends on the energy supplied by the milling medium, the atomic size of the constituents and the thermodynamic properties of the

* Corresponding author. Tel.: +98 9177038948.
E-mail address: amirtaghvaei@gmail.com (A.H. Taghvaei).

0925-8388/$ – see front matter © 2011 Elsevier B.V. All rights reserved.
doi:10.1016/j.jallcom.2011.09.025

alloying system [8]. Schwarz and Johnson developed two criteria for the formation of the amorphous phase during the MA of binary systems [9]; (1) a large negative heat of mixing between the elemental constituents, and (2) a large asymmetry in the diffusion coefficients of the elements are required. An amorphous phase is kinetically produced when the amorphization reaction is much faster than the formation of the crystalline phases [8,9]. It is also demonstrated that during the MA process, the introduction of crystalline defects into the lattice increases the internal energy. When the free energy of the crystal exceeds the free energy of the amorphous phase, the crystalline structure becomes thermodynamically unstable and can be transformed into the amorphous phase [2,10].

Co-based amorphous alloys usually show soft magnetic properties and high mechanical strength [11]. Inoue et al. developed a group of high boron content multicomponent $Co_{40}Fe_{22}M_8B_{30}$ (M = Nb, Zr) soft magnetic glassy ribbons and cylinders with the maximum diameter of 1 mm and a large supercooled liquid region up to 98 K by melt spinning and copper mold casting methods [12]. It has been found that the increase of the boron content up to 30% resulted in an extension of the supercooled liquid region and an increase in the electrical resistivity [6,12]. In addition, cylindrical $Co_{43}Fe_{20}Ta_{5.5}B_{31.5}$ glassy samples with a diameter of 2 mm and a large supercooled liquid region of 72 K prior to crystallization were produced using the copper-mold casting method. This alloy showed ultra high fracture strength above 5 GPa, extremely high permeability of 550,000 and low coercivity of 0.25 A/m [13,14]. Besides it showed the largest supercooled liquid region among the composition range of 5–30 at.% Fe, 4–6 at.% Ta and 20–33 at.% B. Higher Ta content alloy (%Ta > 6) such as $Co_{40}Fe_{22}Ta_8B_{30}$ has not been investigated by the casting methods or the MA process up to now. Some researchers studied the amorphization process in the mechanically alloyed binary Co-based alloys with the boron contents of 20%, 33% and 50% [15,16]. They reported that the Co–B mixture induced solid-state amorphization which becomes faster by increasing the boron content [16]. However, there are only a few studies on the mechanical alloying of the multicomponent Co-based amorphous alloys, especially with a high metalloid content [17]. Fabrication of the high-boron content cobalt-based bulk amorphous alloys by the combination of the MA process and the subsequent consolidation at supercooled liquid region, can present an alternative method to produce the bulk glassy samples in arbitrary shapes and dimensions. But before the consolidation steps, investigation of the powders microstructure, their thermal stability and morphology at different milling times is required. This work investigated the effects of the MA process on phase evolution, amorphous phase formation and its mechanisms in multicomponent $Co_{40}Fe_{22}Ta_8B_{30}$ (at.%) alloy. To the best of the authors' knowledge, no results have been reported by other researchers on this alloy. The powders microstructure at different milling times was characterized by XRD, SEM, TEM and DSC analysis, and the results are discussed in details.

2. Experimental procedure

A high-boron content alloy with a nominal composition of $Co_{40}Fe_{22}Ta_8B_{30}$ (at.%) was prepared by milling of pure elemental Co (Merck, >99.5%, $D_{a.v.}$ = 10 μm), Fe (Merck, >99.5%, $D_{a.v.}$ = 10 μm), Ta (Merck, >99.5%, $D_{a.v.}$ = 40 μm) and B (Merck, >99.5%, $D_{a.v.}$ = 150 μm) powders. MA was performed in a planetary ball mill under the argon atmosphere using a tempered steel vials with a capacity of 80 ml and balls with diameters of 10 and 20 mm at a rotation speed of 310 rpm. The vials were loaded with 10 g powders which were milled at a ball-to-powder mass ratio of 20:1. Experiments were interrupted at some intervals and samples of the milled powder were taken out for characterization.

The phase constituent and structure of the powder particles were investigated by XRD (SHIMADZU Lab X-6000, Cu Kα radiation) and HRTEM (JEOL, JEM 2010). Rietveld-refinements were performed using the MAUD software which is designed to estimate structural parameters such as the crystallite size, the lattice strain and the amount of amorphous phase from the X-ray powder diffraction data [18]. The amorphous phase content of the milled powders was estimated by the Rietveld refinement of the XRD pattern for a mixture of the as-milled powders and the known amount of nanocrystalline Mn powders as a standard. The nanocrystalline Mn powders with an average crystallite size of 13 nm was prepared by ball milling pure Mn (99.5%) for 5 h under the argon atmosphere in a planetary ball mill with the ball-to-powder mass ratio of 20:1. The powder-to-standard mass ratio of 75:25 was used for this purpose. Before mixing, both powders (as-milled Co alloy and Mn standard) were separately sieved and particles smaller than 40 μm were used for the quantitative analysis. The XRD data collections and their quantitative Rietveld analyses were repeated three times in three specimens to check for repeatability and to estimate the potential errors. In the MAUD software, the maximum lattice strain (e) and the average crystallite size (D) of the milled powders were determined by the Double-Voigt approach [19]. For both the quantitative and structural parameters analyses, the fitting process was repeated until the parameter R_b became smaller than 10%.

The morphological change of the powder particles was examined by the scanning electron microscopy (SEM, JEOL-JSM 5310) coupled with the energy dispersive (EDX) analyzer. The thermal stability of the powders was characterized by a differential scanning calorimetry (DSC, NETZSCH, STA 449C Jupiter) with an alumina container under purified argon gas flow. The structure of the as-milled powders, as well as the in situ crystallization behavior were studied by X-ray diffraction in transmission configuration, using a high intensity high-energy monochromatic synchrotron beam (λ = 0.0149 nm) at ID11 of ESRF Grenoble. The heating of the powders sealed under vacuum in a capillary tube was done at a rate of 10 K/min using a LINKAM hot stage mounted perpendicularly to the direction of the X-ray beam.

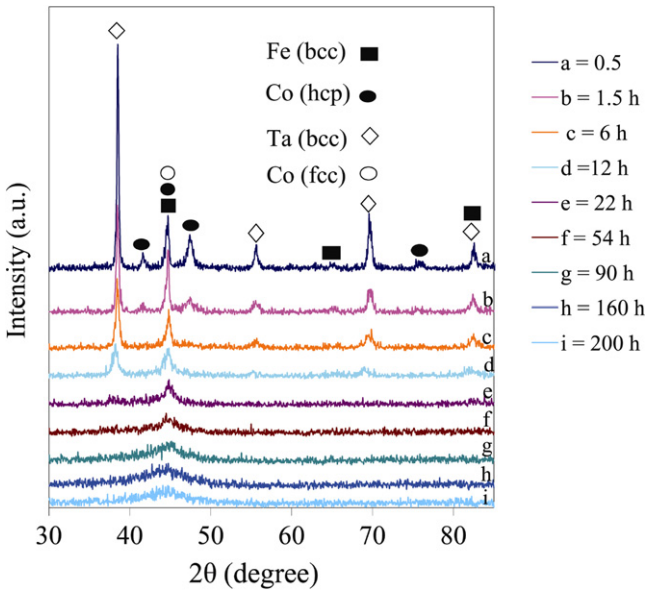

Fig. 1. The XRD patterns of the milled powders after different milling times.

3. Results and discussion

3.1. X-ray analysis

Fig. 1 depicts the XRD patterns of the as-milled powders at different milling times. All the characteristic peaks of the constituent elements are seen at the beginning of milling with the exception of boron, which is a light element and is amorphous in nature. Also, some diffraction peaks of the fcc cobalt are not detected at the early stage of milling. This is due to the allotropic transformation of cobalt from fcc to hcp. Since the fcc cobalt is metastable at room temperature, it turns unstable under applied external mechanical or thermal energy [20]. Hence, this transformation is attributed to a large number of defects created by the severe plastic deformation and the increase of the energy stored in the material during the milling process [20].

According to Fig. 1, alloying of the initial elements after 6 h milling results in a decrease of the bcc tantalum intensity and disappearance of the hcp cobalt diffraction line and consequently the formation of bcc-(Fe, Co) solid solution. Therefore, after 6 h milling, the powders contain dominantly an unreacted tantalum and bcc-(Fe, Co) solid solution. The dissolution of iron, tantalum and boron

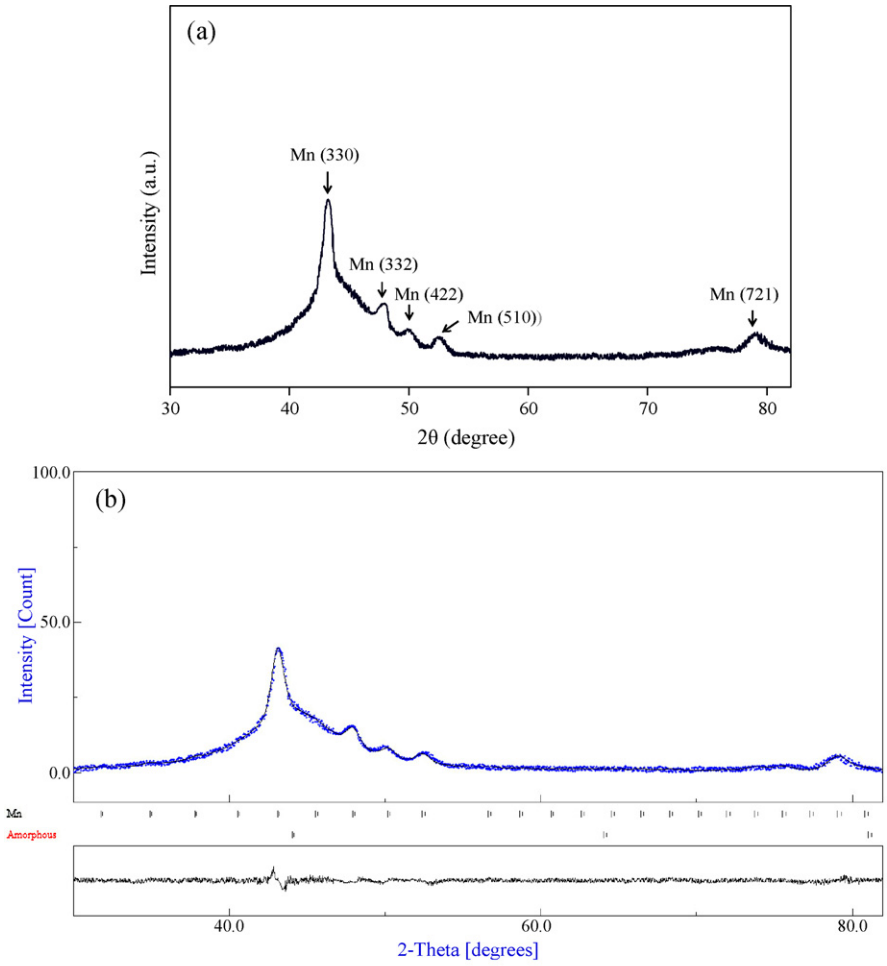

Fig. 2. The XRD pattern of the 200 h milled powder mixed with the nanocrystalline Mn powder (a) and the corresponding curve fitting performed by the Rietveld method (b).

into the cobalt lattice increases the elastic energy for the formation of the solid solution phase due to the size mismatch effect. The lattice mismatch between cobalt and tantalum is higher than the lattice mismatch for cobalt and iron. This means that more elastic energy is needed to dissolve tantalum in the cobalt lattice in comparison to the dissolution of iron. Therefore, dissolution of tantalum needs a longer milling time than that needed for the dissolution of iron into the cobalt lattice. This is the reason for the existence of some unreacted tantalum after 6 h milling. As can be seen in Fig. 1, the XRD pattern of the 22 h milled powders consists of a first order maxima peak attributed to the (1 1 0) plane of the bcc-(Fe, Co) phase superimposed with the halo pattern of the amorphous phase. By further progression of the MA process, broadening of the first-order maximum peak of the bcc-(Fe, Co) phase increases (Fig. 1). This is due to a decrease in the crystallite size, an increase in the lattice strain and/or the existence of a considerable amount of amorphous phase in the structure. At higher milling times (more than 90 h), the halo pattern becomes more pronounced due to the existence of a high amount of amorphous phase in the structure.

Table 1 shows the effect of milling time on the values of 2θ of the (1 1 0) peak of the bcc-(Fe, Co) phase, its crystallite size and lattice strain. After 54 h of milling, due to the existence of a relatively high amount of the amorphous phase in the structure, the major peak of the bcc-(Fe, Co) phase disappeared into the halo pattern. Consequently, the measurement of the mentioned parameters after 54 h of milling is not possible. According to Table 1, the position of the (1 1 0) peak first shifts to the higher 2θ values up to 6 h milling and then decreases to the lower amounts until 54 h milling. Decrease of the lattice parameter during the milling has been reported in other alloys especially with high cobalt concentration [5,21,22]. The lattice contraction could originate from the allotropic phase transformation of cobalt (fcc–hcp) and/or to the triple defect disorder [5,21]. According to Fig. 1, the intensity of tantalum diffraction peaks decreases especially after 6 h milling. Therefore, the substitutional dissolution of tantalum atoms increases the lattice parameter of the bcc-(Fe, Co) phase due to its larger atomic size in comparison with the atomic size of cobalt and iron atoms. Another contribution to the lattice expansion after 6 h milling could be the dissolution of boron atoms on the interstitial sites [23].

Table 1 shows that the average crystallite size rapidly decreases to the nanometric levels by increasing the milling time. The significant grain refinement during the milling process could be explained

Table 1
Variations of crystallite size, lattice strain and diffraction angle 2θ of the first order maximum peak of bcc-(Fe, Co) phase as a function of milling time.

Milling time (h)	Crystallite size (nm)	Lattice strain (%)	2θ of (1 1 0) (°)
0.5	111.43 ± 0.35	0.15 ± 0.03	44.6422 ± 0.0003
1.5	41.35 ± 0.42	0.27 ± 0.05	44.6727 ± 0.0004
6	16.26 ± 0.27	0.62 ± 0.05	44.8041 ± 0.0002
12	9.17 ± 0.31	1.14 ± 0.04	44.7202 ± 0.0005
22	8.45 ± 0.22	1.38 ± 0.06	44.6738 ± 0.0003
54	6.36 ± 0.43	1.60 ± 0.03	44.6344 ± 0.0001

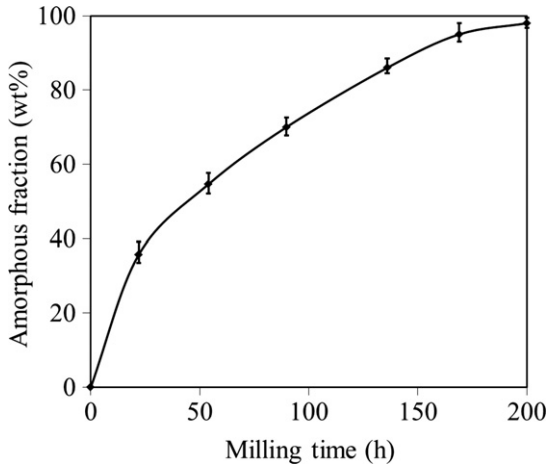

Fig. 3. Variations of amorphous phase fraction (wt%) for the various milling times.

as a result of the severe plastic deformation of the powders as well as the dissolution of boron in the microstructure. Recently, it has been reported that the severe grain refinement could happen by interstitial nitrogen and carbon atoms during MA of Fe–Cr–Mn–N and Fe–C powders, respectively [24,25]. The rapid grain refinement in these alloys was attributed to the segregation of the interstitial nitrogen and carbon atoms into dislocations and grain boundaries, which led to locking of the dislocations and the stabilizing of the grain boundaries [25]. It has been reported that boron atoms could be segregated into the dislocations of α-Fe and established a more strength dislocation locking in comparison with the locking produced by nitrogen and carbon atoms [26]. Thus, it is inferred that the dissolution of boron during the MA process in the structure noticeably decreases the crystallite size by the mechanisms which are very similar to those mentioned for interstitial nitrogen and carbon.

Table 1 also shows the variations of lattice strain during the milling. Lattice strain increases by milling to a value of 1.6% for 54 h milled powders. The increase of the lattice strain can be attributed to the size mismatch effect between the constituents, the increase of the grain boundary fraction and the increase of dislocation density produced by severe plastic deformation [27].

The proportion of the amorphous phase in the as-milled powders was calculated based on the quantitative Rietveld analysis [28,29]. This method can determine the amorphous phase content from the overestimation of an internal crystalline standard in the Rietveld refinement of an appropriate mixture of a standard and the sample powders [29]. The as-milled powders and the nanocrystalline standard Mn powders were mixed in a mass ratio of 75:25, respectively. Fig. 2 illustrates a typical XRD pattern and the corresponding curve fitting performed by the Rietveld refinement method for a mixture of 200 h milled powders and nanocrystalline Mn powders. The fitting process was repeated until the R_b parameter became smaller than 10%. The weight fraction of the amorphous phase based on the mentioned method could be determined from the following equation [28,29]:

$$A = \frac{1-(W_s/R_s)}{100-W_s} \times 10^4\% \quad (1)$$

where A is the weight percentage of the amorphous phase, W_s is the weight concentration of the internal standard (in this study W_s = 25%) and R_s (%) is its Rietveld analyzed concentration [28,29].

Fig. 3 shows the amorphous phase content versus the milling time. According to this figure, the quantity of the amorphous phase first increased sharply and then gradually to the maximum value of 96% after 200 h milling. The formation of the amorphous phase in the present alloying system is due to several effects, such as severe grain size refinement, atomic size effect and the negative heat-of-mixing between the constituents which are explained as follows.

Table 2
Physical parameters and preferred site occupancies in the cobalt lattice of selected elements at room temperature.

Parameter	Co	Fe	Ta	B
μ (GPa)	75	82	69	155
K (GPa)	180	170	200	320
γ	1	0.98	1	1.185
R_B(nm)	0.128	0.126	0.149	0.078
$R = R_B/R_{Co}$	1	0.984	1.164	0.609
Site preference	Base	Substitutional	Substitutional	Interstitial

(a) *Effect of severe grain size refinement*: As discussed previously, dissolution of the boron atoms and the severe plastic deformation of the powders during the milling are responsible for the rapid grain refinement. Ogino et al. [30] proposed that in the milling process, as a result of the grain refinement, the constraints of the neighboring grains are increased. When the grain size is reduced to below a critical size in the order of a few nanometers (possibly <5 nm), the crystallite becomes unstable and the amorphization occurs [28].

(b) *Atomic size effect*: The presence of atoms with different atomic sizes introduces significant strain into the lattice. This increases the strain energy and consequently the free energy of the crystalline phase (to above that of the hypothetical amorphous phase). Since the atomic size effect is less in the amorphous phase than that in the grain boundary and is less in the grain boundary than the crystalline lattice [31], therefore, the thermodynamic stability of the amorphous phase is higher than the grain boundary and that of the grain boundary is higher than the crystallite lattice [31]. Recently, it has been shown that it is possible to determine, at least semi-quantitatively, the contribution of the lattice strain to the solid state amorphization for multicomponent Fe-based alloys by the Egami's model [32]. The Egami's model was developed by Miracle et al. [7,33,34], who introduced the concept of the local clustering of the solvent atoms around the solute atom in order to achieve a dense random packing.According to the Miracle's model, the mean volume strain on the solvent lattice (ε_A^V) in the multicomponent system is calculated from the following equation [34]:

$$\varepsilon_A^V = \frac{\sum_{j=1}^{n} C_j \gamma_j \xi \left[X_{sj}(R_j^3 - 1) + X_{ij}(R_j^3 - \eta^3) \right]}{1 + \sum_{j=1}^{n} C_j X_{sj}(R_j^3 - 1)} \quad (2)$$

where the subscript j denotes a jth alloying element, C_j is the atomic concentration of jth element, R_j is the radius ratio of jth atom, X_{sj} and X_{ij} are the fractions of the solute atoms in the substitutional and interstitial sites. ξ is the coefficient of the compaction of the crystalline lattice. For a close-packed lattice, ξ = 0.74. η is a constant which is 0.414 in the case of the octahedral sites in a close-packed structure. γ_i is given by [34]:

$$\gamma_j = \frac{1 + 4\mu_A/3K_A}{1 + 4\mu_A/3K_j} \quad (3)$$

where μ and K denote the shear modulus and bulk modulus, respectively. Table 2 shows the physical parameters and the preferred site occupancies for the elements of the present study in the Co lattice. Based on Eq. (2), the calculated value of the mean volume lattice strain in the present alloys is 0.065. This value is sufficiently greater than the critical volume lattice strain which is equal to 0.054 [34]. Thus, the calculated volume strain leads to the topological instability of the crystalline lattice and the change of the local coordination number

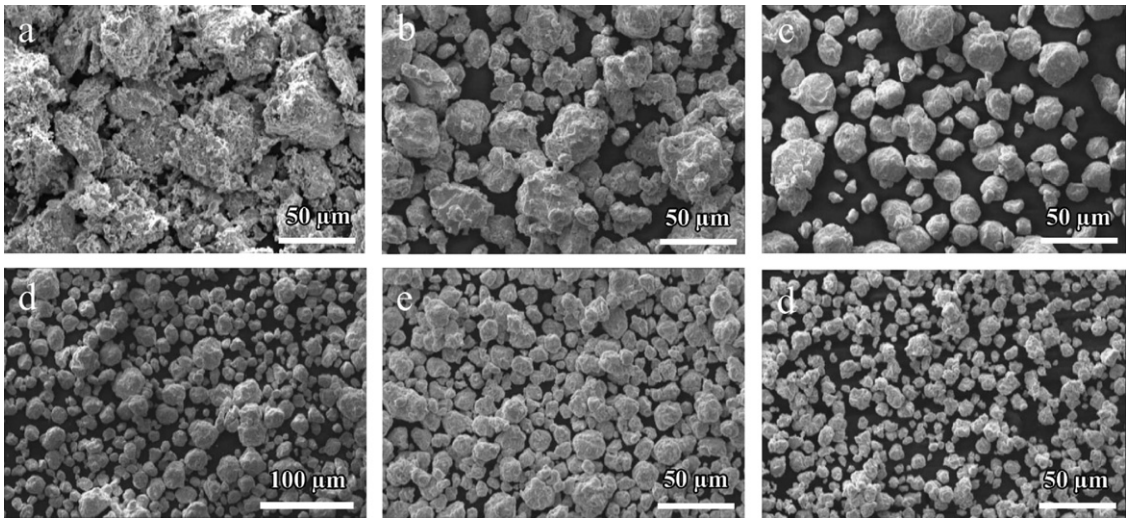

Fig. 4. The SEM micrographs of the powders milled for (a) 1.5 h; (b) 22 h; (c) 54 h; (d) 90 h; (e) 160 h; (f) 200 h.

[34]. This result confirms why the amorphization occurred in the alloy system used in this work. It is worth noting that the mean volume lattice strain for the present alloy is greater than that for rapidly solidified glassy $Co_{43}Fe_{20}Ta_{5.5}B_{31.5}$ alloy ($\varepsilon_A^V = 0.058$) and $Co_{40}Fe_{22}Nb_8B_{30}$ alloy ($\varepsilon_A^V = 0.059$). Therefore, from the atomic size point of view, the alloy in this research has higher tendency to become amorphous in comparison with other mentioned alloys. In addition to the atomic size effect, the MA process introduces crystal defects which raise the free energy of the lattice and contribute to amorphization. However, the atomic size difference is more important in the amorphization process, because the contribution of the lattice defects to increase the energy of the system is rather low, especially for dislocations and vacancies [35].

(c) *Effect of negative heat of mixing*: In the present alloy, the enthalpy of mixing is negative along the major elements as mentioned before. Also, the Ta–B pairs have the largest negative heat of mixing (−54 kJ/mol) through the constituents [36]. This indicates the strong interaction between these two atoms. It has been found thermodynamically that the addition of a third element to Fe–N and Fe–C alloys with strong interaction with nitrogen and carbon, results in a better atomic level intermixing of these solutes and iron during the milling which promotes amorphization [37,38]. Addition of such elements prevents the formation of more stable phases, like nitride and carbide in comparison with the metastable amorphous phase [37,38]. Some investigations have shown that the homogenization and intermixing of boron and some transition metals like iron, cobalt and nickel during the milling did not completely occur at the atomic level by MA [39,40]. Therefore, it may be concluded that the presence of tantalum with high interaction or affinity with boron can improve the intermixing of the mentioned constituent at the atomic level and consequently favors amorphization. It was shown that the metastable amorphous phase during the MA process of Fe–B or Co–B alloys was accompanied by the formation of some borides, such as Fe_2B, FeB and Co_2B [15,16,41]. The addition of some alloying elements like Nb [20] or, as in the present work, Ta, with high affinity to boron, could decrease the activity of boron and prohibits its diffusion over a large distance during MA. This retards the

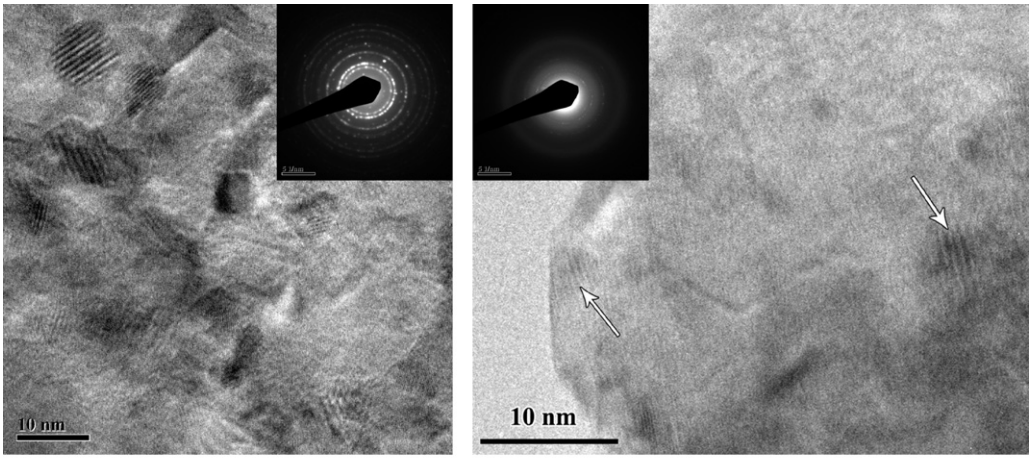

Fig. 5. The HRTEM micrographs and the corresponding SAD patterns of the powder particles milled for (a) 54 h and (b) 200 h.

recovery processes like nucleation and/or growth of more stable phases, such as the formation of borides, which occurs simultaneously with the amorphization reaction in the MA process.

3.2. SEM observations

Fig. 4 shows the SEM micrograph of the powders at different milling times. During the MA process, powder particles are successively flattened, cold welded, fractured and rewelded [5]. At the primary stage of milling, the ductile powder particles are flattened as a result of the compressive force of the ball–powder–ball collisions. Also, the hard and brittle boron particles were fractured to the small particles which agglomerated on the surface of the large and composite powder particles with flattened shape (Fig. 4(a)). By progression of the milling time, the applied intensive shear and impact on the particles lead to the fragmentation of the large and composite particles to the smaller powders with irregular morphology and wide size distributions (Fig. 4(b)). By further milling, the powder particles size and their shape irregularity tend to decrease and the size distribution becomes narrow as illustrated in Fig. 4(c). The development of the MA process decreases the size distribution and increases the homogeneity of the powder particles. Also, the powder particles become more regular in shape (Fig. 4(d) and (e)). By the extension of the MA process up to 200 h, the powder particles become finer, possibly, due to the further development of the amorphous phase in their structure (Fig. 4(f)).

3.3. TEM results

Fig. 5 shows the HRTEM image and the corresponding selected area diffraction (SAD) pattern of the powders at two milling times. For the 54 h milled powders (Fig. 5(a)), the bright field TEM image shows some dark and bright regions. The TEM contrast results from the orientation variations, mass–thickness differences, or dual-structure [28]. The SAD pattern contains the diffraction spots arising from the crystalline regions along with the halo pattern due to the existence of the amorphous phase. Therefore, the SAD pattern confirms that the dark and bright regions of the TEM image are the nanocrystalline phase and an amorphous phase, respectively. Presence of these two phases was confirmed previously by the XRD analysis. According to Fig. 2, the XRD quantitative analysis shows that the fraction of the amorphous phase in the 54 h milled powders is 55% and the average crystallite size of the nanocrystals is 6 nm (Table 1). Thus, both TEM and XRD results are in good agreement. Fig. 5(b) indicates the HRTEM and SAD pattern of 200 h milled powders. As the TEM micrograph shows, the amount of the amorphous phase increases significantly by increasing the milling time from 54 h to 200 h. As explained quantitatively in the previous section, the 200 h milled powders are not fully amorphous and still have some remaining nanocrystals which are indicated by the arrows in the TEM image. This result is confirmed by the SAD pattern which includes small diffraction spots arising from the nanocrystalline regions superimposed on the halo pattern of the amorphous phase. Again, the proportion of the amorphous phase calculated by the XRD analysis could be qualitatively confirmed by the TEM image and its SAD pattern.

3.4. Thermal analysis

In order to investigate the thermal stability of the as-milled powders, differential scanning calorimetry (DSC) was performed at a constant heating rate of 10 K/min under the argon gas atmosphere. Fig. 6 shows the DSC profile of the 200 h milled powders which have the highest amount of amorphous phase. According to this figure, the DSC profile shows a huge and broad exothermic peak, centered around 683 K. By increasing the temperature, a much sharper exothermic peak appears which is attributed to the crystallization of the amorphous phase. According to the DSC profile, the crystallization enthalpy is 47 J/g, and the onset crystallization temperature (T_x) and the peak crystallization temperature (T_p) are 873 K and 904 K, respectively. In order to determine the origin of these reactions, the powders were heated with a constant heating rate of 10 K/min and simultaneously irradiated with a high intensity high-energy monochromatic synchrotron beam ($\lambda = 0.0149$ nm).

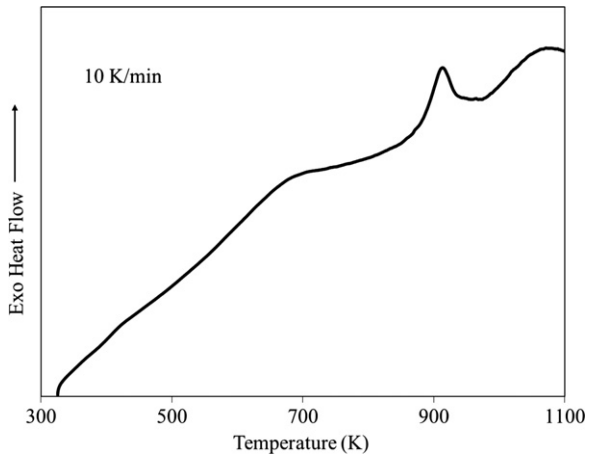

Fig. 6. The DSC profile of the powders milled for 200 h.

Fig. 7(a) depicts the evolution of the XRD pattern of 200 h milled in the temperature range from room up to 973 K. The diffraction patterns are presented as a function of the wave vector Q, which is related to the wavelength λ and to the scan angle θ by:

$$Q = 4\pi \frac{\sin\ \theta}{\lambda} \tag{4}$$

Taking into account the Bragg equation for the first-order reflection:

$$2d\ sin\ \ \theta = \lambda \tag{5}$$

where d is the interplanar spacing of the material, the wave vectors Q is calculated to be:

$$Q = \frac{2\pi}{d} \tag{6}$$

The wave vector depends only on the structure, yielding the same value regardless of the used wavelength. In this way, diffraction patterns recorded with different devices can be easily compared.

According to Fig. 7(a), the powders at room temperature show a diffuse scattering pattern typical for metallic glasses with a maximum at $Q = 31.1\ \text{nm}^{-1}$. As the temperature increases, the amorphous phase of the powders crystallizes and the fraction of crystalline products increases according to the enhancement of their peak intensity. It is also obvious that the crystalline product(s) are stable up to the end of the temperature range. The observation is consistent with the DSC data which exhibits a sharp exothermic peak corresponding to the crystallization reaction.

Fig. 7(b) shows in detail three diffraction patterns, one corresponding to the as-milled powders, one recorded at 773 K (above the first exothermic event) and one at 973 K (above the second exothermic peak). From this figure, the diffuse scattering pattern of the as-milled powders does not show any peaks attributed to the remaining nanocrystalline phases. This result originates from the fact that the average size of the remaining nanocrystals and their fraction is very small as confirmed by the TEM image (Fig. 5).

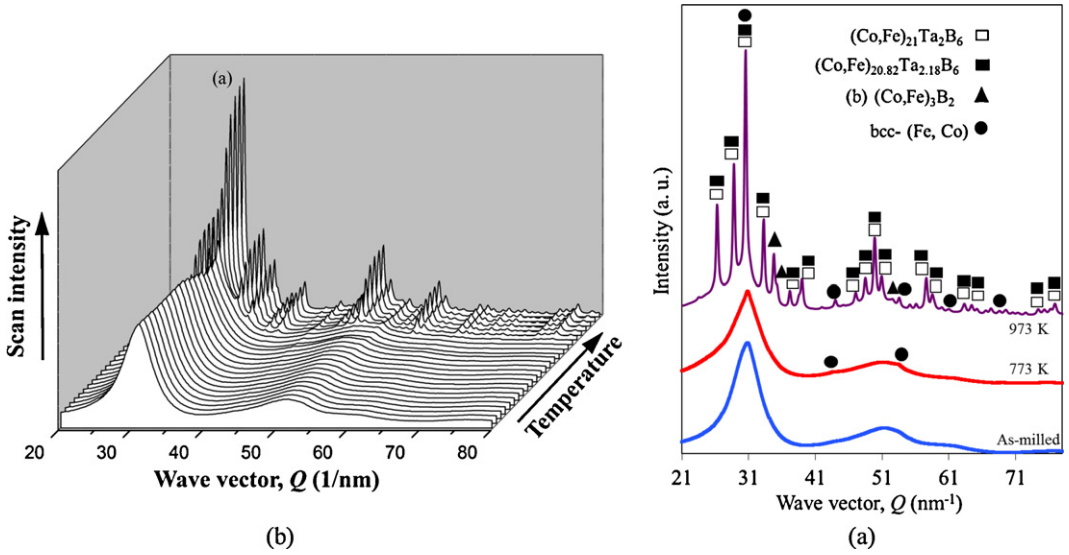

Fig. 7. The evolution of XRD pattern during the in situ heating from room temperature up to 973 K (a) and details at three given temperature (room temperature, 773 K and 973 K) (b).

However, a slight asymmetry of the main broad peak can be observed and this is due to the presence of nanocrystals. The XRD pattern of the powders at 773 K is relatively similar to that of the as-milled powders with the existence of highly weak and broad peaks at 44.1 nm^{-1} and 53.5 nm^{-1}. These peaks are related to the remaining bcc-(Fe, Co) nanocrystals in the amorphous matrix, which have experienced grain growth during the heating. Due to the same effect, the main broad peak becomes a bit sharper. Grain growth, according to the significantly small intensity of the bcc-(Fe, Co) phase, is low, thus, the heat evolved due to the growth process is negligible at 773 K. Therefore, the huge and broad exothermic hump in the DSC profile may arise from other phenomena, such as stress relief and irreversible structural relaxation, i.e. the annihilation of the excess free volume produced during the milling [42]. It is well understood that the heterogeneous deformation of the metallic glasses may generate a large amount of free volume in the shear bands [42]. Therefore, during the milling process, the produced amorphous phase could experience a severe deformation and consequently a large amount of highly localized shear bands and free volume are generated in this phase. Further details of mechanisms and kinetics of structural relaxation in the present alloy is under study.

According to Fig. 6, the as-milled powders do not show a glass transition temperature (T_g). It has been reported that at the presence of a large and broad exothermic peak due to the structural relaxation before the crystallization peak, the exact determination of T_g becomes difficult [43,44]. On the other hand, the small endothermic peak due to the glass transition may be obscured when other heat evolving reactions, such as structural relaxation occur near the T_g [44].

Fig. 7(b) also shows the XRD pattern of the powders heated at 973 K. It shows formation of crystalline products, such as $(Co, Fe)_{20.82}Ta_{2.18}B_6$, $(Co, Fe)_{21}$ Ta_2 B_6 and $(Co, Fe)_3B_2$ phases. These phases confirm that the second exothermic peak in the DSC profile arises from the crystallization of the amorphous phase. Both $(Co, Fe)_{20.82}Ta_{2.18}B_6$ and $(Co, Fe)_{21}$ Ta_2 B_6 phases are complex fcc phases with a large lattice parameter of 1.0552 nm [45]. Therefore, due to the same crystal structure and similar lattice parameter, the peaks of the mentioned metastable phases are overlapped as indicated in Fig. 7(b). These phases can be regarded as isomorphic to the metastable $(Fe, M)_{23}B_6$ (M = Nb, Ta) phase which has been identified as the primary and metastable crystallization products of the bulk glassy Fe–Nb–B and Fe–Nb–Ta–B alloys [14,46]. Similar crystallization products have been reported for the rapidly solidified glassy $Co_{43}Fe_{20}Ta_{5.5}B_{31.5}$ alloy with ultra high strength and large supercooled region [14]. In comparison with the diffraction pattern recorded at773 K, the pattern for the sample at 973 K clearly shows the peaks of bcc-(Fe, Co) phase at wave vectors Q of 30.6, 44.1, 53.5, 61.4 and 68.9 nm^{-1} which results from the growth of pre-existing bcc-(Fe, Co) nanocrystals in the as-milled powders.

Fig. 8(a) illustrates the DSC plots of 200 h milled powders at different heating rates. According to this figure, the peak temperature of crystallization increases from 903 K to 921 K with increase of the heating rate from 5 to 30 K/min. The effective activation energy of the crystallization (E_c) was calculated from the constant heating rate DSC scans in Fig. 8 using the Kissinger method as [47]:

$$\ln\left(\frac{\beta}{T_p^2}\right) = -\left(\frac{E_c}{RT_p}\right) + \text{constant} \tag{7}$$

where β is the heating rate in K/min, T_p is the crystallization temperature in K corresponding to the single crystallization event in the DSC plots and R is the gas constant. The activation energy from the Kissinger plot (Fig. 8(b)) was found to be 640 kJ/mol. It was reported that the activation energy calculated from the crystallization peak temperature by the Kissinger equation is the required activation energy for the growth process [48]. The growth of nuclei requires a long-range atomic rearrangement of constituents, which is closely related to their diffusivity. In the present alloy, the large atomic ratio and strong attractive bonding between the constituents especially between Ta and B atoms decrease the diffusivity and consequently this is responsible for relatively high value of activation energy.

According to Fig. 8(a), the shape of exothermic peaks corresponding to the crystallization event is wide and asymmetrical, with a long high temperature inset and the trailing edge of the peak is steeper than the leading edge. This can be an indication that crystallization itself takes place and results in the formation of a crystalline metastable phase which can transforms into another crystalline phase or the occurrence of two overlapping reactions [49]. According to the literature, metastable $(Co, Fe)_{21}Ta_2B_6$ phase, which is the primary crystallization of the $Co_{43}Fe_{20}Ta_{5.5}B_{31.5}$ glassy alloy tends to transfer to more stable phases like $(Co, Fe)_3B_2$ by increasing the temperature and progress of the crystallization [14].

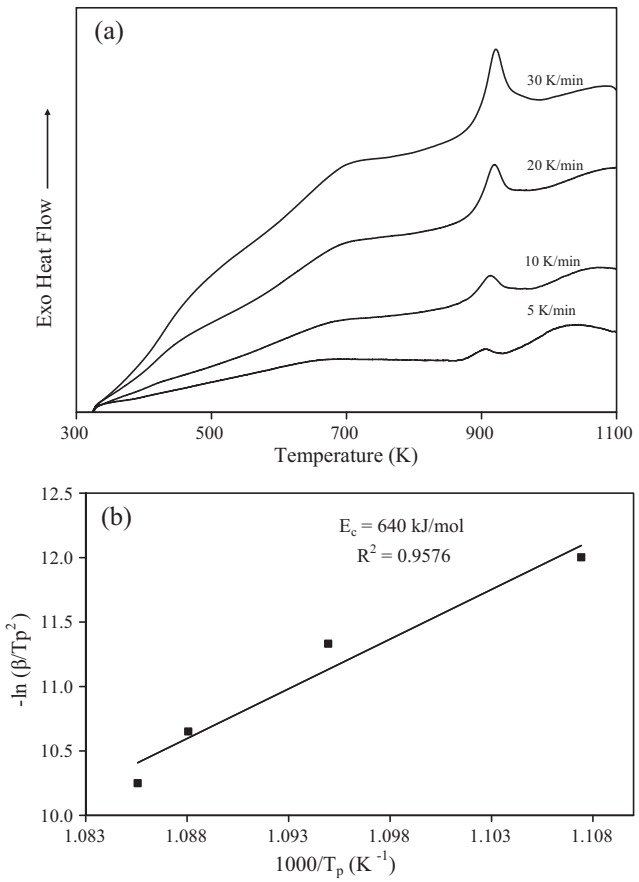

Fig. 8. The DSC curves of 200 h milled powders at different heating rates (a) and the corresponding Kissinger plot (b).

According to Fig. 7(b), the XRD pattern of 200 h milled powders after heating up to the end of crystallization reaction is composed of two metastable phases as well as (Co, Fe)$_3$B$_2$ phase. This result confirms that the metastable (Co, Fe)$_{20.82}$Ta$_{2.18}$B$_6$ and (Co, Fe)$_{21}$ Ta$_2$ B$_6$ phases have a tendency to transfer to the stable phase like (Co, Fe)$_3$B$_2$. Therefore, the calculated activation energy contains two energy contributions, the one necessary to form the primary crystallization phase(s) and another corresponding to a further transformation. As a result, the relatively high value of calculated activation energy is not exotic.

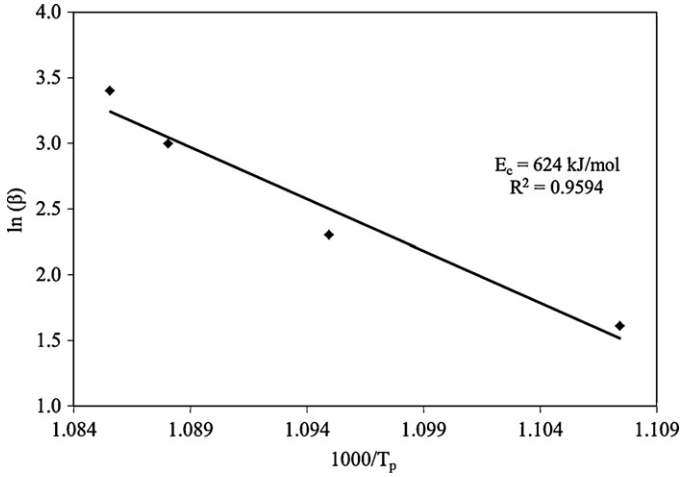

Fig. 9. The Ozawa plot of 200 h milled powders.

Besides the Kissinger method, the Ozawa equation can be used to calculate the activation energy of crystallization which can be expressed as follows [50]:

$$\ln \quad \beta = -1.0516\frac{E_c}{RT_p} + \text{constant} \tag{8}$$

where β and E_c are the heating rate and activation energy, respectively. Fig. 9 depicts the Ozawa plot for 200 h milled powders which indicates the value of activation energy of crystallization is 624 kJ/mol. In comparison with the results derived by the Kissinger equation, the activation energy obtained by the Ozawa method is slightly lower.

4. Conclusions

The MA process of the elemental Fe, Co, Ta and B for the alloy with the nominal composition of $Co_{40}Fe_{22}Ta_8B_{30}$ was investigated. X-ray analysis showed that the MA process at the initial stages led to the formation of the bcc-(Fe, Co) phase as well as some unreacted Ta. Further milling resulted in a significant decrease in the major peak intensity of bcc-(Fe, Co) and increased its broadening due to the grain refinement, introduction of lattice strain and development of the amorphous phase. The reasons for the rapid grain refinement were explained based on the severe plastic deformation and dissolution of boron in the powder particles. The quantitative XRD analysis based on the Rietveld refinement showed that the amorphous phase increased by the progress of the milling and finally its weight fraction reached 96% within 200 h, being verified by TEM observations. The amorphization mechanisms were discussed in terms of extreme grain refinement, atomic size effect and concept of local topological instability developed by Miracle and the heat of mixing consideration. Results of the DSC test indicated that the large structural relaxation was followed by the crystallization of the amorphous phase through a single exothermic peak with the onset temperature of 873 K. The microstructural evolution of the powders from the as-milled up to the devitrified state was investigated by the X-ray diffraction in transmission configuration using synchrotron radiation. These XRD results of the crystallized powders confirmed the formation of metastable complex fcc phases like (Co, Fe)$_{20.82}$Ta$_{2.18}$B$_6$ and (Co, Fe)$_{21}$ Ta$_2$ B$_6$ in addition to the (Co, Fe)$_3$B$_2$ phase. These results were similar to the crystallization products of the rapidly solidified glassy alloys with the same constituent elements and similar composition, which were reported by other workers.

Acknowledgments

The authors thank Shiraz University for financial support and technical assistance and Dr. Rasool Amini for fruitful discussions. One of the authors (M.S.) acknowledges the support of the German Science Foundation (DFG) through grant STO 873/2-1 and of the European Synchrotron Radiation Facility (ESRF) for the experiment HD 482.

References

[1] C.A. Schuh, T.C. Hufnagel, U. Ramamurty, Acta Mater. 55 (2007) 4067–4109.
[2] A. Inoue, C. Suryanarayana, Bulk Metallic Glasses, CRC Press, Boca Raton, NY, 2011.
[3] B. Movahedi, M.H. Enayati, C.C. Wong, Mater. Sci. Eng. B 172 (2010) 50–54.
[4] P.Y. Lee, C.K. Lin, I.K. Jeng, C.C. Wang, G.S. Chen, Mater. Chem. Phys. 84 (2004) 358–362.
[5] C. Suryanarayana, Prog. Mater. Sci. 46 (2001) 1–184.
[6] S.N. Kane, A. Gupta, Z. Gercsi, F. Mazaleyrat, L.K. Varga, J. Magn. Magn. Mater. 292 (2005) 447–452.
[7] D.B. Miracle, Acta Mater. 54 (2006) 4317–4336.
[8] J.M. Gonzalez, G.A. Perez Alcazar, E. Ligia, J.A. Zamora, A. Tabares, J.R. Bohorquez, Gancedo, J. Magn. Magn. Mater. 261 (2003) 337–346.
[9] R.B. Schwarz, W.L. Johnson, Phys. Rev. Lett. 51 (1983) 415–418.

[10] C. Suryanarayana, S. Sharma, J. Appl. Phys. 104 (2008) 103503–103511.
[11] M.E. McHenry, M.A. Willard, D.E. Laughlin, Prog. Mater. Sci. 44 (1999) 291–433.
[12] T. Itoi, A. Inoue, Mater. Trans. JIM 41 (2000) 1256–1262.
[13] B.L. Shen, H. Koshiba, A. Inoue, H.M. Kimura, T. Mizushima, Mater. Trans. JIM 42 (2001) 2136–2140.
[14] A. Inoue, B.L. Shen, H. Koshiba, H. Kato, A.R. Yavari, Acta Mater. 52 (2004) 1631–1637.
[15] A. Corrias, G. Ennas, G. Marongue, G. Paschina, J. Mater. Sci. 26 (1991) 5081–5084.
[16] A. Corrias, G. Ennas, G. Marongiu, A. Musinu, G. Paschina, J. Mater. Res. 8 (1993) 1327–1333.
[17] H.M. Wu, C.J. Hu, H.C. Li, J. Alloys Compd. 483 (2008) 553–556.
[18] L. Lutterotti, MAUD CPD Newsletter (IUCr) 24, 2000.
[19] D. Balzar, N. Audebrand, M. Daymond, A. Fitch, A. Hewat, J.I. Langford, A. Le Bail, D. Louër, O. Masson, C.N. McCowan, N.C. Popa, P.W. Stephens, B. Toby, J. Appl. Crystallogr. 37 (2004) 911–924.
[20] S. Allega, S. Azzaza, R. Bensalem, J.J. Suñol, S. Khene, G. Fillion, J. Alloys Compd. 482 (2009) 86–89.
[21] H. Moumeni, S. Alleg, J.M. Greneche, J. Alloys Compd. 286 (2005) 12–19.
[22] M. Eskandarani, Mechanical Alloying for Fabrication of Advanced Engineering Materials, William Andrew, 2001, p. 2.
[23] S. Sharma, C. Suryanarayana, Scripta Mater. 58 (2008) 508–511.
[24] R. Amini, E. Salahinejad, M. Marasi, T. Sritharan, Mater. Sci. Eng. A 527 (2010) 1135–1142.
[25] E.P. Yelsukov, G.A. Dorofeev, A.V. Zagainov, N.F. Vildanova, A.N. Maratkanova, Mater. Sci. Eng. A 369 (2004) 16–22.
[26] I. Codd, N.J. Petch, Philos. Magn. 5 (1960) 30–42.
[27] Y.J. Liu, I.T.H. Chang, Acta Mater. 50 (2002) 2747–2760.
[28] R. Amini, M.J. Hadianfard, E. Salahinejad, M. Marasi, T. Sritharan, J. Mater. Sci. 44 (2009) 136–148.
[29] R.S. Winburn, D.G. Grier, G.J. Mccarthy, Powder Diffr. 15 (2000) 163–172.
[30] Y. Ogino, T. Yamasaki, S. Murayama, R. Sakai, J. Non-Cryst. Solids 117–118 (1990) 737–740.
[31] Y. Ogino, S. Murayama, Y. Yamazaki, J. Less-Common Met. 168 (1991) 221–235.
[32] T. Egami, Y. Waseda, J. Non-Cryst. Solids 64 (1990) 113–134.
[33] D.B. Miracle, O.N. Senkov, Mater. Sci. Eng. A 347 (2003) 50–58.
[34] O.N. Senkov, D.B. Miracle, J. Non-Cryst. Solids 317 (2003) 34–39.
[35] S. Sharma, R. Vaidyanathan, C. Suryanarayana, Appl. Phys. Lett. 90 (2007) 111915–111918.
[36] A. Takeuchi, A. Inoue, Mater. Trans. JIM 46 (2005) 2817–2829.
[37] H. Miura, K. Omuro, H. Ogawa, ISIJ Int. 36 (1996) 951–957.
[38] K. Qmuro, H. Miura, Appl. Phys. Lett. 64 (1994) 2961–2963.
[39] H. Okumura, K.N. Ishihara, P.H. Shingu, H.S. Park, S. Nasu, J. Mater. Sci. 27 (1992) 153–160.
[40] T. Nasu, M. Sakurai, K. Suzuki, C.C. Koch, A.M. Edwards, D.E. Sayers, Mater. Trans. JIM 36 (1995) 1088–1090.
[41] P. Ruuskanen, O. Heczko, J. Non-Cryst. Solids 224 (1998) 36–42.
[42] P.E. Donovan, W.M. Stobbs, Acta Metall. 29 (1981) 1419–1436.
[43] H.W. Jin, Y.J. Kim, C.G. Park, J. Mater. Sci. 36 (2001) 2089–2094.
[44] X.D. Liu, M. Nagumo, M. Umemoto, Mater. Sci. Eng. A 252 (1998) 179–187.
[45] P. Villars, L.D. Calvert, Pearson's Handbook of Crystallographic Data for Intermetallic Phases, vol. 2, ASM International, Materials Park, OH, 1991, p. 1428.
[46] M. Imafuku, S. Sato, H. Koshiba, E. Matsubara, A. Inoue, Mater. Trans. JIM 41 (2002) 1526–1529.
[47] H.E. Kissinger, Anal. Chem. 29 (1957) 1702–1706.
[48] H.R. Wang, Y.L. Gao, G.H. Min, X.D. Hui, Y.F. Ye, Phys. Lett. A 314 (2003) 81–87.
[49] M. Stoica, S. Kumar, S. Roth, S. Ram, J. Eckert, G. Vaughan, A.R. Yavari, J. Alloys Compd. 483 (2009) 632–637.
[50] T. Ozawa, Bull. Chem. Soc. Jpn. 38 (1965) 1881–1886.